J. Fluid Mech. (1992), *vol.* 242, *pp.* 51–78
Printed in Great Britain

Stochastic backscatter in large-eddy simulations of boundary layers

By P. J. MASON AND D. J. THOMSON
The Meteorological Office, London Road, Bracknell, Berks, RG12 2SZ, UK

(Received 25 June 1991 and in revised form 4 February 1992)

The ability of a large-eddy simulation to represent the large-scale motions in the interior of a turbulent flow is well established. However, concerns remain for the behaviour close to rigid surfaces where, with the exception of low-Reynolds-number flows, the large-eddy description must be matched to some description of the flow in which all except the larger-scale 'inactive' motions are averaged. The performance of large-eddy simulations in this near-surface region is investigated and it is pointed out that in previous simulations the mean velocity profile in the matching region has not had a logarithmic form. A number of new simulations are conducted with the Smagorinsky (1963) subgrid model. These also show departures from the logarithmic profile and suggest that it may not be possible to eliminate the error by adjustments of the subgrid lengthscale. An obvious defect of the Smagorinsky model is its failure to represent stochastic subgrid stress variations. It is shown that inclusion of these variations leads to a marked improvement in the near-wall flow simulation. The constant of proportionality between the magnitude of the fluctuations in stress and the Smagorinsky stresses has been empirically determined to give an accurate logarithmic flow profile. This value provides an energy backscatter rate slightly larger than the dissipation rate and equal to idealized theoretical predictions (Chasnov 1991).

1. Introduction

In most turbulent flows the transports of heat and momentum are dominated by large-scale motions whose properties depend on some integral characteristics of the flow. As a result time-average closure techniques which depend on local mean gradients are often inadequate, whilst large-eddy simulations offer the potential for accurate predictions. A large-eddy simulation involves calculating the large-scale turbulent motions explicitly with a three-dimensional numerical model whilst the smaller-scale motions are parametrized. In the flow interior, away from boundaries and significant statically stable stratification, this approach seems both rational and is in practice insensitive to the details of the parametrization of small-scale motions. The rationality arises when the distinction between the large-scale (resolved-scale) and parametrized motions (subgrid-scale) falls within an inertial subrange. In such cases theory (e.g. Lesieur 1987) and results from applications (Bardina, Ferziger & Reynolds 1983) suggest that a simple eddy viscosity may provide an adequate parametrization (subgrid-scale model). Bardina *et al.*'s work shows that in these cases it makes little difference whether the eddy viscosity varies in proportion to the local deformation (the Smagorinsky 1963 model), or takes a constant value corresponding to an ensemble mean of the local Smagorinsky model values. The mean viscosities from the Smagorinsky model vary slowly in flow interiors and in these regions the

large-eddy simulation of a high-Reynolds-number flow will have the character of a moderate-Reynolds-number flow with the eddy viscosity giving the moderate 'Reynolds' number. A so-called direct simulation considers a numerical representation of a true moderate-Reynolds-number flow with a constant molecular viscosity. The critical differences between a large-eddy simulation of a high-Reynolds-number flow and a moderate-Reynolds-number direct simulation thus arise near the boundary and in regions of strong static stability. In these regions the characteristic scale of the turbulence reduces to values less than the size of the mesh spacing and the magnitude of the implied eddy viscosity will reduce. In the present study attention will be confined to the near-surface region and the problem of statically stable flow will not be dealt with. Since the behaviour in the region near a surface determines the main difference between a high-Reynolds-number simulation and one of only moderate Reynolds number, it is crucial that this behaviour is correct. Existing boundary conditions and near-wall subgrid models are based on results from time-averaged flows and their application to large-eddy simulations is uncertain.

Previous studies have used high-resolution large-eddy simulations to examine whether subgrid models are adequate in the flow interior (Bardina *et al.* 1983). A comparison was made between stress values averaged over a number of mesh points and stress values obtained by applying the subgrid model to fields averaged over these points. It was found that the instantaneous stresses were much larger than those implied by the Smagorinsky model. Since the subgrid motions are only considered to be averaged over a scale comparable to the largest subgrid scale, such large instantaneous stresses are expected just from the point of view of statistical stability. However, in the flow interior of a typical large-eddy simulation the amount of energy occurring on the subgrid scale is usually only about 15% of the total energy. The interior subgrid fluxes (of scalars and momentum) are only about 3% of the total fluxes. Such values confirm that the typical flow interior mesh sizes are smaller than the scales involved in turbulence energy production and lie within at least the start of the inertial subrange. This and the insensitivity of results to the subgrid-scale model give confidence that, in spite of the lack of statistical fluctuations in the modelled subgrid stress, the simulation is reliable in the flow interior.

The modelling of the near-surface region differs considerably from the modelling of flow interior. In most large-eddy simulations the mesh spacing parallel to the surface is constant with distance from the boundary whilst the mesh is usually refined in the vertical close to the surface. This refinement does not allow the resolution of the truly three-dimensional motions which occur on a decreasing scale as the surface is approached, but is essential to allow a proper resolution of quasi-two-dimensional motions which occur near the surface and which derive from the 'interior' eddies. The limit to model representation of three-dimensional motions is set by the resolution parallel to the boundary. The subgrid model and/or boundary conditions near the surface thus need to represent the near-surface eddies whose scale varies in proportion to distance from the surface. On the one hand this can be anticipated to be difficult as, in contrast to the flow interior, it involves the main production scale. On the other hand there are some encouraging factors. At these heights there is a local balance between the ensemble-average turbulence energy production and dissipation. Near the surface, the characteristic scale of the turbulent motions becomes smaller than the scale of numerical mesh parallel to the surface, and with this implied volume averaging there is some hope of the subgrid stresses becoming deterministic functions of the resolved velocity as the surface is

approached. The gravest difficulties can be anticipated to be at the 'matching' height at which the magnitudes of the resolved and subgrid stresses are comparable. At this height the worst of everything prevails. The subgrid stresses are large and would be expected to have statistical fluctuations.

In this paper we confine attention to the simulation of equilibrium boundary layers in flows with arbitrarily high Reynolds number. The specific boundary conditions chosen concern infinite-Reynolds-number flow over a rough surface, but an analogous model would apply to high-Reynolds-number flow over a smooth surface. We begin by examining a typical simulation with a Smagorinsky subgrid model. The simulation fails to maintain the correct logarithmic flow profile in the matching region, the velocity gradient in this region being too great. A series of simulations with varying resolution and a different near-surface mixing-length descriptions were conducted to try to improve the flow profile in the matching region. Section 2 presents the large-eddy model used for these studies and §3 the results. No adequate solution to the difficulties was found. In §4 a stochastic subgrid model is proposed and the results obtained with this are presented in §5. These results show a marked improvement in the near-wall mean velocity and temperature profiles. Finally in §6 conclusions are given.

2. Model description

The large-eddy simulation technique used in the present study is, apart perhaps from the boundary conditions, fairly standard and is based on the Smagorinsky (1963) subgrid model. Conceptually we consider spatially filtered velocity and scalar fields and seek to solve the set of continuous equations obtained by applying this filter operation to the Navier–Stokes equations, i.e.

$$\frac{\partial u_i}{\partial t}+\frac{\partial u_i u_j}{\partial x_j}=-\frac{\partial p}{\partial x_i}-\delta_{i1}\frac{\partial P}{\partial x_1}+\frac{\partial \tau_{ij}}{\partial x_j}, \tag{1}$$

$$\frac{\partial \theta}{\partial t}+\frac{\partial u_i \theta}{\partial x_i}=-\frac{\partial H_i}{\partial x_i}, \tag{2}$$

$$\frac{\partial u_i}{\partial x_i}=0, \tag{3}$$

where $(u_1, u_2, u_3) = (u, v, w)$ are the components of the (filtered) velocity $\boldsymbol{u}$ and θ is a passive scalar that will be included in some of the simulations; u is the component in the streamwise or x-direction, v is the component in the spanwise or y-direction, and w is the component in the vertical or z-direction, i.e. the direction normal to the non-slip boundary; p is the pressure or, more correctly, pressure divided by density – however, to simplify the language we will suppress mention of the density both here and below (or, equivalently, choose units of mass so that the density is unity). A fixed mean pressure gradient $\partial P/\partial x$ is included, τ_{ij} is the subgrid stress tensor and H_i the subgrid scalar flux vector. Some of the simulations described below are intended to represent a planetary boundary layer; for these simulations a term $\boldsymbol{u} \wedge \boldsymbol{k}f$, where k is a vertical unit vector and f is the Coriolis parameter (10^{-4} s^{-1}), is added to the right-hand side of (1) to represent the Coriolis force, and the mean pressure gradient is applied in the y-direction instead of the x-direction (so that the geostrophic wind is aligned with the x-axis).

In order to close equations (1)–(3) we need a model for $\boldsymbol{\tau}$ and $\boldsymbol{H}$. The more usual deterministic models employ either a high-order closure or a local equilibrium limit

of such a closure, essentially the Smagorinsky model. From past studies it is clear that the Smagorinsky model is usually adequate and certainly the best understood model. It will be adopted in the present study, i.e.

$$\tau_{ij} = \nu\left(\frac{\partial u_i}{\partial x_j}+\frac{\partial u_j}{\partial x_i}\right), \tag{4}$$

$$H_i = -\frac{\nu}{Pr}\frac{\partial \theta}{\partial x_i}, \tag{5}$$

where the eddy viscosity ν is given by

$$\nu = l^2 S \tag{6}$$

and

$$S^2 = \frac{1}{2}\left(\frac{\partial u_i}{\partial x_j}+\frac{\partial u_j}{\partial x_i}\right)^2. \tag{7}$$

Here Pr is a Prandtl number, taken to be 0.7, and l is a lengthscale. Note that the modelled subgrid stress tensor is traceless – the isotropic part can be regarded as being absorbed in a redefinition of the pressure. In the interior of the flow (the near-surface behaviour will be considered below) l is set equal to a constant lengthscale l_0 which according to the theoretical arguments of Lilly (1967), we may relate to a filter scale l_f by $l_f = l_0/C_f$, where C_f is about 0.2 and depends upon the exact form assumed for the filter operation. However, it is important to note that the form of the filter seen by the resolved motions is determined by the subgrid model and not by any particular assumed form for the filter. The Smagorinsky model only involves a single scalar parameter l_0 which describes the scale of the as yet unknown filter which the Smagorinsky model gives.

At this stage we are not concerned with finite-difference implementation but merely with the continuous equations. A characteristic of the near-wall region is that the lengthscale of the subgrid-scale motions will not be given by a constant value of l_0 but will decrease as the wall is approached. Specifically, with a no-slip condition of $\boldsymbol{u} = 0$ at $z = 0$ and a roughness length z_0, we have

$$\nu = \kappa^2(z+z_0)^2 S \tag{8}$$

for $(z+z_0) \ll l_0$, where κ is the von Kármán constant. This provides a rational boundary behaviour which is both consistent with the Smagorinsky model in form and which, in the limit $(z+z_0) \ll l_0$, is correctly deterministic in character. In this limit we are dealing with the average of three-dimensional eddies of scale $\sim (z+z_0)$ in a volume $\sim l_f^3$ and the resulting stress should be a deterministic function of the filtered velocity field. The remaining problem concerns the match between the near-surface region and the interior. Here we shall consider simple but arbitrary matches such as

$$1/l^n = 1/l_0^n + 1/(\kappa(z+z_0))^n, \tag{9}$$

where n is a constant.

Equations (1)–(7) and (9) together with (i) a choice for l_0, (ii) the boundary condition $\boldsymbol{u} = 0$ at $z = 0$, and (iii) the boundary conditions at the top of the domain, provide a complete definition of the model problem. Since it will be advantageous in a practical simulation, it is useful to ask whether the logarithmic boundary condition could be explicitly implemented at some height, i.e.

$$\tau = \frac{1}{M^2}|v(z)|v(z), \tag{10}$$

where
$$M = \frac{1}{\kappa}\ln(1+z/z_0), \tag{11}$$

$v(z)$ is the horizontal velocity at a height z and τ is the surface stress vector. Similar equations apply to θ. Clearly this will be valid as z approaches z_0 and will be invalid far above the boundary (owing to fluctuations in v which are imperfectly correlated with fluctuations in the surface stress), but the maximum height at which it can be correctly applied needs to be determined.

For (10) to be equivalent to the application of the mixing-length relation (9) on a refined mesh, the difference in stress between the surface and height z must be much less than the variations in surface stress. From the (resolved) momentum equation we note this stress difference is related to the (resolved) time change, advection and pressure gradient terms. In the flow interior such terms are in rough balance and have similar values, but as the non-slip surface is approached the pressure gradient persists whilst the other terms fall to zero. At the surface the vertical gradient of the shear stress must equal the local resolved horizontal pressure gradient and the departure of the stress between its surface value and the value a small height z above the surface will be $\sim z\partial p/\partial x$, where $\partial p/\partial x$ is the typical magnitude of the horizontal pressure gradient. In most problems the fluctuating pressure gradient is greater than the mean pressure gradient and, as noted, the surface values will be typical of those in the flow interior, i.e. $\sim u_*^2/L$ where u_* is the square root of the surface stress (a scale for the velocity fluctuation) and L is the lengthscale for differentiating the pressure fluctuations and is expected to be of order l_f. As noted above, for accurate application of (10) we require the stress change $\sim zu_*^2/L$ to be less than the variations in surface stress. If we assume resolved velocity fluctuations of size $\sim u'(z)$ at the height z we can use (10) to estimate the magnitude of the stress fluctuations as $\sim u_*^2 u'(z)/U_0(z)$, where $U_0(z)$ is the mean flow profile. The requirement for using (10) then becomes $zu_*^2/L \ll u_*^2 u'(z)/U_0(z)$, i.e. $z \ll \delta_e$, where δ_e is defined by $\delta_e \sim Lu'(\delta_e)/U_0(\delta_e)$. Now we expect $u'(z)$ to vary logarithmically below δ_e and to be of order u_* at a height $\sim L$. This leads to $u' \sim u_* \log(z/z_0)/\log(L/z_0)$ and

$$\delta_e \sim L/\log(L/z_0). \tag{12}$$

The scale, δ_e, can be physically identified with the characteristic diffusion height scale of variations on a scale L and it is also relevant in boundary-layer problems involving flow over undulations or roughness changes (see e.g. Wood & Mason 1991). However it is difficult in practice to make this estimate quantitative. The recommended procedure is to check that the height of application of (10), the surface value of $\partial p/\partial x$ and the standard deviation of the surface stress σ_τ satisfy

$$z\partial p/\partial x \ll \sigma_\tau. \tag{13}$$

To obtain the variance of the velocity components and of θ, diagnostic estimates of the subgrid contributions are required. These are obtained by assuming that the subgrid energy E is isotropically distributed among the three velocity components and by adopting the following estimates of E and the scalar variance E_θ:

$$\epsilon = C_1\frac{E^{\frac{3}{2}}}{l}, \quad \epsilon_\theta = D_1\frac{E^{\frac{1}{2}}E_\theta}{l}. \tag{14}$$

Here ϵ and ϵ_θ are the rates of dissipation of energy and half the scalar variance by

viscosity and molecular diffusivity. If, consistent with the Smagorinsky model, we assume a local balance between production and dissipation of subgrid energy, ϵ and ϵ_θ are given by νS^2 and $\nu D^2/Pr$ respectively, where D^2 is the square of the local temperature gradient. Also $C_1 = a^3$ and $D_1 = Pra_\theta^4/a$, where a^2 is the stress–energy ratio and a_θ^2 is the correlation coefficient for the heat flux vector, defined by $a_\theta^4 = |\boldsymbol{H}|^2/(E_\theta E)$ (values of $a^2 = 0.3$ and $a_\theta^2 = 0.45$ are taken from inertial sub-range arguments, Mason 1989). We note that there is some uncertainty over the validity of these values. The inertial subrange arguments (based on the approach of Lilly 1967) contain many assumptions and, in any case, we have not adopted the value of Pr (and hence of D_1) implied by these arguments. Also, the arguments break down in the near-surface region where the subgrid scales are no longer isotropic and C_1 and D_1 may not be constant.

Having presented the problem in continuous equations the problem of implementing a finite-difference solution remains. The representation in finite-difference form introduces the parameter $C_s = l_0/\Delta$, where Δ is a typical mesh spacing (wherever a quantitatively precise value of Δ is needed, it will be defined to be $(\Delta x\,\Delta y\,\Delta z)^{\frac{1}{3}}$). Although, on the assumption that $\Delta = l_f$, C_s has been regarded as a fundamental constant, here we follow Mason & Callen (1986) and recognize that, with l_0 selected, C_s is only a measure of numerical resolution. Large values of C_s (greater than about 0.2) provide smooth well-resolved solutions with little finite-difference error ($l_f \geqslant \Delta$), whilst smaller values give rough solutions with finite-difference errors ($l_f \leqslant \Delta$). In practice a fixed number of mesh points are available to most studies and unduly large values of C_s will restrict the range of scales simulated to the detriment of the results. Optimum results are likely to be obtained with C_s small enough to give finite-difference errors no greater than the errors implicit in the formulation of the subgrid model. This value is a matter of judgement and may vary from problem to problem if the scale of the subgrid motions extends close to the energy-producing scales. In the present study a range of values close to 0.2 will be considered. A Galilean transformation is used to reduce the Courant-number limitations on the timestep, with the equations being solved in a frame moving at the average of the maximum and minimum horizontally averaged velocities (excluding the surface level where $\boldsymbol{u} = 0$).

In principle the implementation of boundary conditions presents no finite-difference problems, but using fine vertical resolution close to boundaries has direct penalties in its use of mesh points. In the present study the computational boundary condition which is applied is thus equation (10) above. The height at which it is applied is such that (13) is satisfied and the effective near-wall behaviour does not differ significantly from that obtained with good resolution down to the surface and direct application of the no-slip condition. Other aspects of this boundary condition and differences between the von Kármán constant implied by the instantaneous and the time-averaged velocity profiles are discussed by Mason & Callen (1986).

The numerical methods used are also discussed by Mason & Callen (1986) but the details of the results depend on the methods adopted and the essential features will be noted again. The numerical procedure, which uses a staggered mesh, is second-order accurate in space on grids with slowly varying vertical mesh spacings and uses a form of the nonlinear terms (Piacsek & Williams 1970) which, with the leapfrog time-marching scheme, ensures energy and scalar variance conservation properties. The values of the deformation S and the eddy viscosity ν are evaluated and stored on w-points so as to avoid averaging of important z-derivatives in the z-direction. Although not useful in all flows, this choice provides an improved accuracy in

boundary-layer flows of the type considered here. For numerical stability the viscous terms are advanced in time with a simple forward timestep.

Noting that the aim of the present study is to consider, in particular, the match between the interior flow and the near-surface boundary conditions, attention is confined to flows in which a boundary layer with logarithmic flow profile is expected. These simulations have been conducted with compromises that should not affect the present study but that are not ideal for study of the whole boundary layer.

The first flow considered is a neutral static stability planetary boundary layer. These simulations involve a Coriolis term and a consequent long timescale for geostrophic adjustment. They also have a tendency to show deep large-scale motions. In the present simulations these effects have been reduced by applying the boundary conditions $u = U_g$, $v = 0$, $w = 0$ (and $\theta = 0$ for the passive scalar) at the top of the domain. Here U_g is the geostrophically balanced velocity expected well above the boundary layer. The lateral boundaries are considered periodic. The height of the top of the domain has been chosen so as to correspond roughly to the expected height scale of the stress variation. The specific parameters selected are a surface roughness length z_0 of 0.1 m and $U_g = 10$ m s^{-1} with a domain depth of 1200 m, a domain length in the x-direction of 3200 m and a lateral domain width of 1600 m. In this restricted size of domain the direct influence of the Coriolis term is limited to the mean flow. The number of grid points is modest i.e. $40 \times 40 \times 24$ in the x-, y- and z-directions but allows a reasonable simulation that is broadly comparable with the more detailed simulations of Mason & Thomson (1987). The z-direction mesh has a variable spacing with smaller grid intervals close to the surface. The passive scalar is introduced into these simulations by imposing a constant surface flux H_0. With an imposed flux the logarithmic surface boundary condition for the scalar is only required for diagnostic estimates of the surface value of the scalar field. The value of l_0 used is 10 m and C_s has a value of about 0.2 in the lower third of the domain but decreases to about 0.15 close to the upper boundary. The height of the lowest grid point above the surface is about 5 m.

The second flow considered is very similar but lacks the small complicating influence of the Coriolis term. The flow considered is turbulent flow in a horizontally infinite channel with a stress-free (but rigid) upper surface and constant imposed pressure gradient. The lower rigid non-slip surface is taken as rough with the same value of z_0, i.e. 0.1 m, as used in the planetary-boundary-layer case. The channel depth up to the free-surface boundary conditions ($\partial u/\partial z = \partial v/\partial z = 0$, $w = 0$) has been taken as 1000 m. In order to provide high spatial resolution of the eddies, critical in determining the lower part of the boundary layer, the length of the domain has been limited to 1000 m and the width to 600 m. This will clearly cause the loss of significant larger-scale eddies and this must be noted in considering the results. The number of mesh points used is $54 \times 54 \times 64$ so that relative to the planetary-boundary-layer simulation the resolution has been increased by a factor of about 4 in all three directions. In the interior of the flow Δz is 19 m, with most of the mesh refinement occurring below 200 m. The height of the lowest grid point above the surface is about 0.6 m. The various simulations used values of l_0 varying from 2 m to 5 m, corresponding to values of C_s (based on the grid spacing in the interior) between about 0.13 and 0.32.

The initial conditions for the simulations were given by the solution of a one-dimensional mixing-length model with random perturbations added. The model running procedures including timestep determination were as used by Mason & Callen (1986). The results shown here were all obtained after periods of at least $5\delta/u_*$

from the initial conditions, where δ is the boundary-layer depth and u_* is the square root of the mean surface stress. The results shown are subsequent averages over periods of approximately $2\delta/u_*$.

3. Smagorinsky model results

We first consider the neutral static stability planetary-boundary-layer simulation with the standard Smagorinsky subgrid model and a mixing-length profile given by (9) with $n = 2$. For the purpose of checking on the match between the flow interior and the wall region, this simulation can be considered similar to past high-Reynolds-number simulations of boundary layers in which a logarithmic velocity profile is expected. The shear stress profiles (figure 1) show a steady decrease of $\overline{uw}$ with height; this is of course an inevitable consequence of momentum budget considerations. The values of $\overline{vw}$ are somewhat smaller and are caused by the influence of the Coriolis term. These flow statistics were obtained after a simulation time of about 6 h and the mean flow is still evolving slowly on the Coriolis timescale. The adjustment timescale for the turbulence is much more rapid than the Coriolis timescale and the turbulence approximates to a steady state.

Figure 2 shows the variances σ_u^2, σ_v^2 and σ_w^2 of the velocity components in this flow. A diagnostic estimate of the subgrid-scale variances has been obtained using (14) and the assumption of equal energy in each component. This is not an adequate diagnostic estimate close to the surface but it is reasonable in the flow interior. The σ_w^2 profile in particular shows an unrealistic local minimum close to the surface. With allowance for this deficiency, the values of σ_v^2 and σ_w^2 are in rough agreement with observations but the σ_u^2 profile close to the surface shows an unrealistic elevated maximum. There are two factors which seem likely to contribute to this error. Close to the surface the eddy structure in this simulation (see e.g. Mason & Thomson 1987) shows distinct elongated structures which are similar in character to the near-surface streak structure correctly seen in low-Reynolds-number simulations (Moin & Kim 1982). However, in reality the expected flow structure in the logarithmic region is of eddies which have a self-similar structure with height. Hence, as a result of the self-similar smaller-scale eddies which are unresolved in the model, there may be a further tendency to transfer energy from u into the other flow components which is not present in the model. With the application of a filter to this self-similar structure, the occurrence near the surface of streak structures of fixed scale is not surprising, but perhaps resembles a low-Reynolds-number simulation with a viscosity numerically equal to the subgrid-scale turbulent diffusivity of the large-eddy simulation. This is a rather loose argument but it seems wise to express concern that the character of the near-surface flow seems to match observations of low-Reynolds-number flows. The other factor is more definite in its diagnosis. Figure 3 shows the vertical profiles of non-dimensional velocity shear S_v and passive scalar gradient S_θ in the lowest third of the boundary layer, where S_v and S_θ are defined by

$$S_v = \left(\left(\frac{\partial \bar{u}}{\partial z}\right)^2 + \left(\frac{\partial \bar{v}}{\partial z}\right)^2\right)^{\frac{1}{2}} \frac{\kappa(z+z_0)}{u_*},$$

$$S_\theta = \frac{\partial \bar{\theta}}{\partial z} \frac{\kappa(z+z_0)}{\theta_* Pr} \frac{u_* \theta_* (\overline{uw}^2 + \overline{vw}^2)^{\frac{1}{2}}}{\overline{w\theta} u_*^2},$$

with $\theta_* = -H_0/u_*$. These quantities should take a value of unity within the strict near-surface logarithmic layer. Over the depth of the boundary layer the shear stress

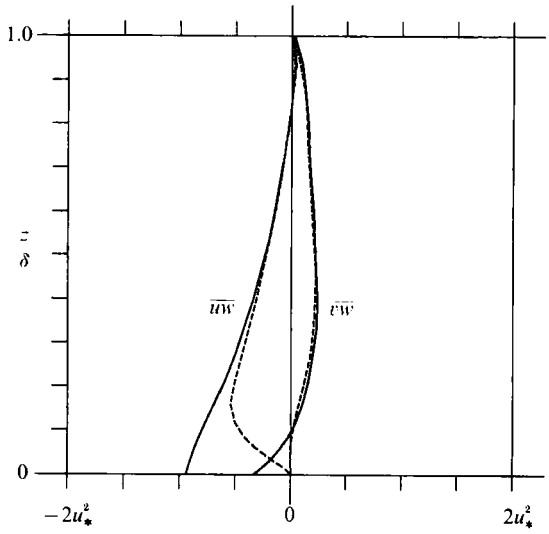

FIGURE 1. Shear stress profiles, $\overline{uw}$ and $\overline{vw}$, from the planetary-boundary-layer simulation without backscatter. Solid lines: total stress; dashed lines: resolved part.

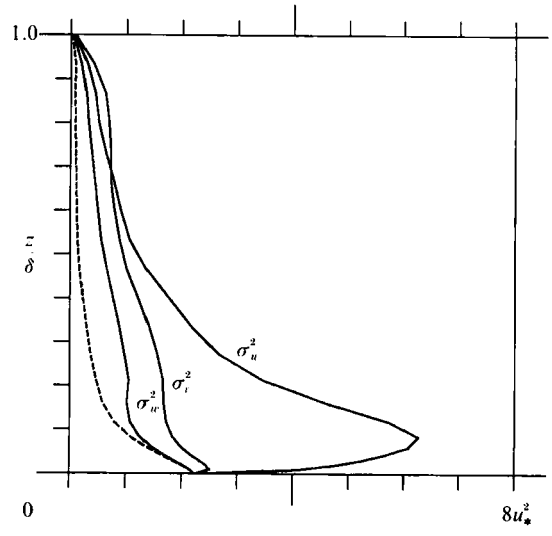

FIGURE 2. Profiles of the velocity variances σ_u^2, σ_v^2 and σ_w^2 from the planetary-boundary-layer simulation without backscatter. Solid lines: total variance; dashed line: subgrid part. The subgrid contributions to each variance are assumed equal and calculated from (14).

decreases to zero whilst, in consequence of the constant scalar upper boundary condition, the scalar flux does not vary. To make the values of S_v and S_θ comparable S_θ has been defined with the factor $u_*\theta_*(\overline{uw}^2+\overline{vw}^2)^{\frac{1}{2}}/u_*^2\,\overline{w\theta}$, where $\overline{uw}$, $\overline{vw}$ and $\overline{w\theta}$ are the horizontally averaged values of the (subgrid plus resolved) shear stress and scalar flux. If the flux–gradient relation between the horizontally averaged gradients and fluxes of the scalar is the same (apart from a Prandtl-number correction) as that for velocity, this factor will make $S_v = S_\theta$. Pr here refers to the Prandtl number for all the turbulence; however, we adopt the same value as used in the subgrid model (0.7) in calculating S_θ. For further reference the non-dimensional shear obtained from a

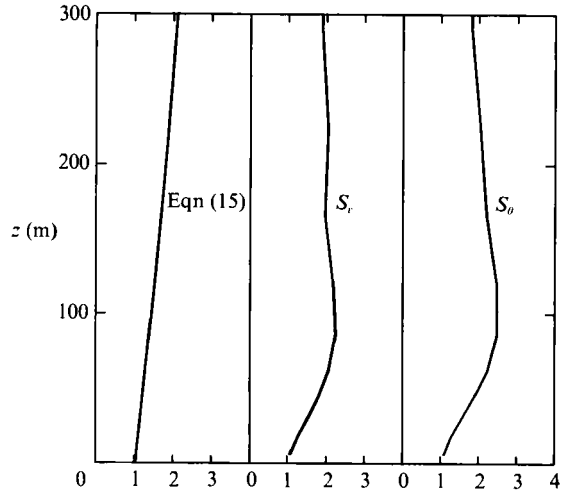

FIGURE 3. Profiles of the non-dimensional shear and passive scalar gradient from the planetary-boundary-layer simulation without backscatter. Also shown is the non-dimensional shear obtained from a mixing-length solution with the mixing length given by (15).

mixing-length solution of the channel flow problem described in §2 is also shown (the channel and planetary-boundary-layer flows are of course expected to be very similar near the surface). The mixing length l has been given by

$$\frac{1}{l} = \frac{1}{\kappa(z+z_0)} + \frac{1}{l_m} \tag{15}$$

with $l_m = 80$ m. This mixing-length solution is shown to illustrate what might be considered an acceptable variation of non-dimensional shear within the nominally logarithmic region. The simulation results show, for both the velocity and scalar profiles, a severe error. The non-dimensional shear shows a maximum value of about 2 at a height of order the characteristic height of the matching region. This excessive value of $\partial\bar{u}/\partial z$ is certain to have contributed to the excessive values of σ_u^2 which are also dominant at this height. It is also certain to have contributed to errors in global quantities such as the drag coefficient.

Noting that the shear stress profile is forced by momentum budget considerations to be realistic we can comment on what features of the simulation may have caused the problem. The most trivial cause would be too small a value of subgrid-scale mixing length in the matching region. If the resolved motions remain unchanged then a correct velocity profile must be obtainable by use of a suitable value of mixing length. The other cause might be the resolved motions. Two not entirely separate changes to the resolved motions might resolve the problem. First, an increase in the resolved $\overline{uw}$ would cause the subgrid part of $\overline{uw}$ to reduce and hence would reduce the mean velocity gradient. Alternatively an increase in the size of the resolved motion deformation would, for fixed subgrid mixing length and mean velocity gradient, lead to an increased subgrid shear stress. However, because the shear stress profile is forced to be realistic, the subgrid stress cannot increase and so the mean velocity gradient would decrease. Similar considerations apply to the passive scalar gradients.

The errors discussed here, are, we believe, detectable in all past high-Reynolds-number simulations of comparable boundary layers. Such simulations start with the

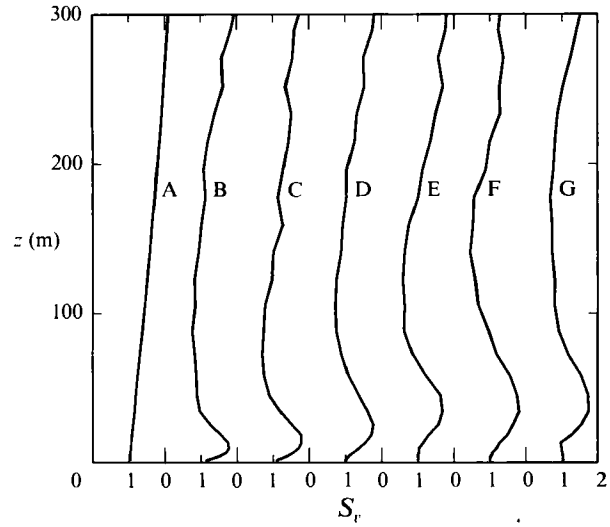

FIGURE 4. Profiles of the non-dimensional shear from simulations of flow in a free-surface channel (without backscatter). Profile B is from a simulation with $l_0 = 2$ m and $n = 1$; C is with $l_0 = 3$ m and $n = 1$; D is with $l_0 = 3$ m and $n = 2$; E is with $l_0 = 3$ m and with $l = \kappa(z+z_0)/[1+h^3/(6+h)]^{\frac{1}{3}}$, where $h = \kappa(z+z_0)l_0$, replacing equation (9); F is with $l_0 = 5$ m and $n = 2$; G is with $l_0 = 5$ m and $n = \infty$; A is the non-dimensional shear obtained from a mixing-length solution with the mixing-length given by (15).

results of Deardorff (1970) and include the coarse-resolution solutions in the work of Piomelli, Moin & Ferziger (1988). Previous results with a refinement of the near-wall resolution show similar excessive gradients in the matching region to those shown here. Past results from simulations with no mesh refinement at the wall simply show an excessive gradient between the two grid points nearest the wall. Low-Reynolds-number large-eddy simulations such as those considered by Piomelli *et al.* (1988) do not suffer from this problem. This is most probably just a consequence of the full resolution of the near-wall turbulence which occurs in these cases; close to the wall the subgrid viscosity becomes less than the molecular viscosity and so the simulation is essentially a direct simulation. Such high resolution of wall regions is not possible in high-Reynolds-number flows such as the atmospheric boundary layer and it is clear that the problem must be solved to allow satisfactory application of large-eddy simulations to high-Reynolds-number flows.

In order to investigate this problem a series of simulations of infinite-Reynolds-number turbulent flow in a free-surface channel flow were conducted as described above in §2. From these simulations we will only present the profiles of non-dimensional velocity gradient in the lowest third of the channel depth. The first question to address is whether the error will vanish as the resolution increases. Profile D in figure 4 is from a simulation with the same form for the profile of l as used with the planetary-boundary-layer simulation but the filter scale and mesh spacings are a factor of about 3–4 smaller. The velocity profile shows a qualitatively similar error but the height scale over which it occurs is reduced and the size of error is also slightly reduced. In consequence of these quantitative changes the solution is more satisfactory but the error remains substantial and still distorts the σ_u^2 profile to give an unrealistic maximum close to the surface.

Velocity profiles B, C, D, F and G show the consequence of varying the power n in (9) and of varying the filter scale with fixed mesh spacing. These changes alter the

height scale of the error but none produce a marked improvement. Profile E has been obtained in a simulation using a mixing-length function derived empirically from the simulation giving profile C. Given the resolved motion characteristics of that simulation, the mixing-length profile required to give the expected velocity profile has been estimated and approximated with a fit to a simple function. The resulting l-profile actually exceeds l_0 in the matching region. If the resolved motion did not change, this new l-profile would give the desired velocity profile. In fact the large values of $\partial\overline{u}/\partial z$ occur at a higher height as the increased lengthscales damp the turbulence and increase the height of the matching region. The error has not been significantly reduced.

From these tests we are forced to the view that perhaps no mixing-length variation with height would be satisfactory. No proof of this can be given but the tests point strongly to this conclusion. In the matching region the simulation seems to lack resolved stress. A possible physical process whose omission may have caused this problem is the expected statistical fluctuations in subgrid stress. Fluctuations in subgrid stress will scatter energy from the subgrid scales to the resolved scales. This process is further likely to be of maximum importance precisely in the matching region where the subgrid stresses are large but the subgrid lengthscale is still comparable with the scale of the filter operation. We will now present a proposal for adding these stress fluctuations to our subgrid model and then present results obtained with this 'stochastic backscatter'.

4. Backscatter model

It has long been recognized that subgrid-scale stresses should have stochastic fluctuations and that these fluctuations lead to a backscatter of energy from the subgrid scales (e.g. Leslie & Quarini 1979; Kraichnan 1976). In a spectral representation this arises through the interaction between the sub-filter-scale wavenumbers which transfers energy to resolved-scale wavenumbers. In physical space the process is simply seen as fluctuations in the subgrid stresses. Recent work (Chasnov 1991) has sought to calculate this backscatter in an inertial subrange using EDQNM theory. Such theory is important in confirming that the approach adopted here is reasonable, but it could not easily, in itself, be applied to the present problem. Other recent work (Leith 1990) parallels the present work more closely in providing an implementation in a large-eddy simulation of an anisotropic flow but does not engage the issue of dealing with the near-surface region of a boundary layer. In the flow interior the model detailed here is essentially the same as that proposed by Leith. Given the common desire to link with the Smagorinsky model and the expected spectral form of the backscatter, this similarity is inevitable. In the present study the intention is to incorporate backscatter in the wall region of the flow. In this region the subgrid scales no longer correspond to an inertial subrange and the theoretical basis is consequently weaker. The model proposed is in essence based on physical and dimensional reasoning.

In physical space we can consider a filter and regard the velocity field as divided into a filtered part $\langle u\rangle$ and a fluctuation or subgrid part $u-\langle u\rangle$. These fluctuating parts give rise to the subgrid stresses. A deterministic subgrid model relates such subgrid stresses to the gradients of the resolved $\langle u\rangle$, $\langle v\rangle$ and $\langle w\rangle$ fields. The Smagorinsky model is a mixing-length implementation of this determination and, in the absence of subgrid-scale transport processes, provides a drain of energy whose magnitude seems reasonable in the mean. If we consider that the subgrid-scale eddies

have a characteristic lengthscale l_e and characteristic timescale T, then, from consideration of the statistics of forming the average stress over a filter-volume of scale l_f from eddies of scale l_e, the variance of the filtered stress (for a fixed resolved velocity field) will, for $l_e \ll l_f$, be proportional to $(l_e/l_f)^3 u_{*1}^4$, where u_{*1} is a local subgrid turbulent velocity scale. Differentiating on a scale l_f leads to fluctuations in the gradients of the filtered stresses of size

$$\frac{l_e^{\frac{3}{2}}}{l_f^{\frac{5}{2}}} u_{*1}^2. \tag{16}$$

Also, if l_e is of order l_f we expect the variance of the filtered stress to be of order u_{*1}^4 and the gradients in the filtered stresses to be of order u_{*1}^2/l_f. In both cases the stress will vary on a timescale T. (Note that if we consider a sharp 'top-hat' spatial filter, then the appropriate average stress is an area average, because the rate of change of filtered velocity at a point is related to the stresses on the *surface* of the top-hat region surrounding the point. This leads to a stress variance of order $(l_e/l_f)^2 u_{*1}^4$ for $l_e \ll l_f$ and stress gradients of order $(l_e/l_f)\, u_{*1}^2/l_f$. In this case the size of the stress gradients cannot be so easily estimated from the variance of the top-hat filtered stresses (namely $(l_e/l_f)^3 u_{*1}^4$) because the top-hat filter is a somewhat singular case, having a long tail in spectral space which results in the contributions to the gradients of the top-hat filtered stress being dominated by scales which are much smaller than the filter scale.)

It is now possible to estimate the rate of energy backscatter resulting from the fluctuations in stress. We assume the fluctuating stress gradients, and hence the resultant accelerations, have magnitude

$$a \propto \frac{l_e^{\frac{3}{2}}}{l_f^{\frac{5}{2}}} u_{*1}^2. \tag{17}$$

This is consistent with the above analysis for $l_e \ll l_f$ and for l_e of order l_f. These accelerations are expected to vary on a timescale T, giving an input to the resolved energy K given by

$$\frac{\partial K}{\partial t} \propto a^2 T \propto \frac{l_e^3}{l_f^5} u_{*1}^4\, T. \tag{18}$$

We note that $T \propto l_e/u_{*1}$ and the dissipation $\epsilon \propto u_{*1}^3/l_e$. Thus (18) yields

$$\frac{\partial K}{\partial t} \propto \frac{l_e^5}{l_f^5} \epsilon. \tag{19}$$

Note that T is of the order of the local viscous stability limit on the timestep.

We assume the filter scale l_f is constant throughout the flow. In particular we will assume that l_f does not alter as the wall is approached. The value of l_f is not formally known but is assumed proportional to l_0, the value in the flow interior of the mixing length in the Smagorinsky model. We also assume the size l_e of the subgrid eddies is proportional to the subgrid-scale mixing length l by a similar constant of proportionality. The backscatter model will be required to give an energy backscatter rate with a pointwise mean value of

$$\frac{\partial K}{\partial t} = C_B \left(\frac{l}{l_0}\right)^5 \epsilon. \tag{20}$$

Here C_B is a constant which, as we note below, theory suggests should be about unity in value.

For a scalar variable we assume a flux variance

$$\sigma^2_{\text{flux}} \propto \frac{l_e^3}{l_f^3} u_{*1}^2 \theta_{*1}^2, \tag{21}$$

where θ_{*1} is a local scale for the magnitude of the subgrid scalar fluctuations. An analogous argument then leads to an input to the resolved scalar variance K_θ given by

$$\frac{\partial K_\theta}{\partial t} = \frac{l_e^3}{l_f^5} u_{*1}^2 \theta_{*1}^2 T_\theta, \tag{22}$$

where T_θ is the timescale for variations in the scalar fluxes and may be different from T. Finally we obtain

$$\frac{1}{2}\frac{\partial K_\theta}{\partial t} = C_{B\theta}\left(\frac{l}{l_0}\right)^5 \epsilon_\theta \tag{23}$$

where for consistency $C_{B\theta}$ is defined relative to half the scalar variance. The factors of $(l/l_0)^5$ obtained in (20) and (23) are only based on simple arguments, valid in a limit which does not really apply, and must be treated with caution. Comments on the relative size of C_B and $C_{B\theta}$ are made below.

Considering the application of the filter operation to a turbulent flow, it is physically clear that if the filter is applied to widely separated flow volumes then the values of the fluctuations in the (filtered) subgrid stress will be uncorrelated. If however we consider points closer in space than the filter scale, the subgrid stress fluctuations will be correlated. We therefore expect the fluctuating stresses to vary on the filter scale. On scales greater than the filter scale the random stress values imply an energy backscatter with a k^4 spectrum in accord with theoretical expectations (Kraichnan 1976).

Guided by the above we will introduce random stresses and scalar fluxes into our simulations to provide backscatter of energy and scalar variance. The stress fluctuations give rise to a force but only the divergence-free part of this force need be considered – unless we are concerned over the exact value of model pressure we do not have to consider the irrotational part of the force which can be absorbed in the pressure gradient by a redefinition of pressure. In the model we will therefore introduce a random vector potential (ϕ_x, ϕ_y, ϕ_z) and the random accelerations will be given by the curl of this vector potential. In the scalar equations we will introduce a random flux vector (ψ_x, ψ_y, ψ_z) with the random source of the scalar field being given by its divergence. In the implementation we take six three-dimensional fields of independent random numbers defined on the numerical grid. These fields should then be scaled appropriately and filtered on the filter scale to obtain the components of the vector potential and flux vector. However, as we have noted, the filter is not known. Here we filter by applying a 1:2:1 smoothing operator in all three directions. This generates an acceleration spectrum which falls off in a reasonable way at high wavenumbers. There is a further complication where the mesh is non-uniform. For example close to the wall the mesh is refined and this filter operation will not correspond to the required fixed scale. To compensate for this we adjust the scaling of the random numbers so that the energy input will not depend on the local mesh spacing. In a similar way we hope that the exact frequency of the energy input is not

critical and impose the random accelerations not on a timescale T, but on a timescale equal to the timestep Δt. To maintain the same energy input and ensure consistent behaviour as $\Delta t \to 0$ we must again adjust the scaling appropriately. Although we will aim to enforce the desired rate of energy backscatter we are failing to ensure that the accelerations which give this backscatter are always on the correct space and time scales.

We can now describe the whole procedure in the numerical model. First, fields of uniformly distributed random numbers with mean zero are generated. Because a leapfrog numerical time-marching scheme is used, these random numbers are changed only every other timestep to avoid excessive time-splitting. These fields are scaled appropriately (as indicated below), filtered with the three-dimensional 1:2:1 operator, and then the curl (divergence in the scalar case) of the resulting field is taken to give the required acceleration field a_i (or scalar source q). As noted above, the scalings of the filtered random numbers should be chosen to ensure the desired backscatter rates. The accelerations give rise to a local rate of change of resolved energy K whose ensemble average (conditional on the values of the resolved fields) is given by

$$\frac{\partial K}{\partial t} = (\sigma_{a1}^2 + \sigma_{a2}^2 + \sigma_{a3}^2)\,\Delta t, \tag{24}$$

where σ_{ai}^2 is the variance of a_i. Similarly the ensemble average rate of change of scalar variance is given by

$$\frac{\partial K_\theta}{\partial t} = 2\sigma_q^2\,\Delta t, \tag{25}$$

where σ_q^2 is the variance of q. To ensure the desired energy input at each point, the random-number scaling factor is chosen to be position dependent. This factor does not vary between components but is of course different for the vector potential and the flux vector. The factor is chosen to ensure that the right-hand sides of (24) and (25) equal the desired backscatter rates of energy and scalar variance, i.e. $C_{\mathrm{B}}(l/l_0)^5\epsilon$ and $2C_{\mathrm{B}\theta}(l/l_0)^5\epsilon_\theta$. In implementing this, ϵ is calculated using (29) below.

In the results presented below, the filtering was (incorrectly) carried out before the scaling. This has the effect of altering the backscatter rates slightly because the values of σ_{ai} and σ_q then depend on the gradients in the scaling factors as well as on the local pointwise values. However, subsequent tests have shown that the backscatter rate was only altered by a few percent and that the flow statistics were not significantly affected.

The preceding conceptual discussion of the backscatter can provide some comment on the ratio $C_{\mathrm{B}}/C_{\mathrm{B}\theta}$. In the interior of the flow, we have $\sigma_{\mathrm{stress}} = \alpha_{\mathrm{s}}(\frac{2}{3}E)$ and $\sigma_{\mathrm{flux}} = \alpha_{\mathrm{f}}(\frac{2}{3}E)^{\frac{1}{2}}E_\theta^{\frac{1}{2}}$, where α_{s} and α_{f} are order unity (they are exactly unity for statistics of pointwise stresses and fluxes in isotropic quasi-Gaussian flows). Following the above analysis and differentiating the stress and flux fields on a scale l_{f}, we obtain

$$\frac{\partial K}{\partial t} \propto \frac{\sigma_{\mathrm{stress}}^2\,T}{l_{\mathrm{f}}^2} \propto \alpha_{\mathrm{s}}^2(\tfrac{2}{3}E)^2 T/l_{\mathrm{f}}^2 \tag{26}$$

and

$$\frac{\partial K_\theta}{\partial t} \propto \frac{\sigma_{\mathrm{flux}}^2\,T_\theta}{l_{\mathrm{f}}^2} \propto \alpha_{\mathrm{f}}^2(\tfrac{2}{3}E)\,E_\theta\,T_\theta/l_{\mathrm{f}}^2. \tag{27}$$

The following argument suggests that the constants of proportionality in (26) and (27) are likely to be similar. There are three components of the random flux while

there are nine components of the random stress. However one third of the velocity modes excited by the random stresses are compressible modes which are suppressed by the pressure, and an additional factor of a half is expected in (26) because K is $\frac{1}{2}\overline{\boldsymbol{u}^2}$, not $\overline{\boldsymbol{u}^2}$. Equations (26) and (27) can be combined with (14), (20), (23) and the assumption of equal constants in (26) and (27) to obtain

$$C_{\mathrm{B}\theta} = C_{\mathrm{B}} \frac{3C_1 T_\theta \alpha_{\mathrm{f}}^2}{4D_1 T \alpha_{\mathrm{s}}^2}. \tag{28}$$

If we take $\alpha_{\mathrm{s}} = \alpha_{\mathrm{f}}$, $T = T_\theta$, and note the proposed numerical values of C_1 and D_1, then $C_{\mathrm{B}\theta} = 0.40 C_{\mathrm{B}}$. Although there are many assumptions in this argument we are left with the view that $C_{\mathrm{B}\theta}$ is most probably less than C_{B}. If we could estimate α_{s}, α_{f}, T, T_θ and the effect of differentiation more accurately we could estimate C_{B} and $C_{\mathrm{B}\theta}$ as well as their ratio. The above analysis does confirm however that they are formally of order unity.

A more convincing but still approximate estimate can be obtained from EDQNM theory (Chasnov 1991). Using the backscatter expressions in Chasnov (1991) a value of $C_{\mathrm{B}} = 1.4$ is obtained for an infinite inertial subrange (J. R. Chasnov, private communication). Noting the differences between momentum and scalar transfer in EDQNM theory (Lesieur 1987) the value for $C_{\mathrm{B}\theta}$ would be expected to be reduced in consequence of the smaller scalar timescale. Specifically $C_{\mathrm{B}\theta}/C_{\mathrm{B}} = \frac{10}{7}(\beta/\alpha)(\frac{1}{3}Pr)$, where α and β are the inertial-subrange constants for velocity and temperature (see Appendix A). Taking $\alpha = 1.5$, $\beta = 0.7$ and $Pr = 0.7$ gives $C_{\mathrm{B}\theta} = 0.32 C_{\mathrm{B}}$. This agrees qualitatively with the preceding assertions for $C_{\mathrm{B}\theta}/C_{\mathrm{B}}$.

In this study C_{B} is found to have profound effects and we are able to see what value of C_{B} gives the best results. As we shall see below, the value $C_{\mathrm{B}} = 1.4$, when used with $n = 2$ in (9), has been found to give optimal results. Owing to the various assumptions in the implementation this empirically determined value should not be considered precise. We are however encouraged by the evidence that C_{B} is about unity and in agreement with Chasnov's value. Owing to the passivity and linearity of the scalar variable the value of $C_{\mathrm{B}\theta}$ does not affect the mean velocity or scalar profiles and the only basis for empirical adjustment would be statistics involving the scalar variance. Noting the uncertainty in $C_{\mathrm{B}\theta}$ we consider various values including $C_{\mathrm{B}\theta} = 0$, the latter case simply allowing a judgement of the separate effects of scalar backscatter and momentum backscatter.

The introduction of backscatter has some penalty in increasing the computational cost of the simulation. In an initial implementation the CPU time per timestep was nearly doubled. Most of this increase arose from the calculation of random numbers and the CPU penalty was reduced to an increase of only 15% in the CPU time by re-using the same two-dimensional field of random numbers. Each required two-dimensional field of random numbers was then obtained by considering a random origin within this periodic two-dimensional field. On every alternate timestep however, completely new random numbers were generated. Tests were carried out in which energy was introduced into an initial state with $\boldsymbol{u} = 0$ by applying random forcing as indicated above (but with the right-hand side of (20) replaced by a constant). These tests showed the ensemble-average energy backscatter rate to be unchanged by this computational short cut. There is a further possible penalty if the timestep is liable to be limited by viscous numerical instabilities. Although the mean values of viscosity are not much altered, the peak values within the fields were increased by a factor of about two. This leads to some reduction in timestep in the case considered below.

Before proceeding with the model we need to consider whether the inclusion of backscatter implies that the subgrid Prandtl number should be altered and also how the subgrid-scale energy and scalar variance should be estimated. The local equilibrium subgrid energy equation with backscatter is

$$\nu S^2 = \epsilon + C_B \left(\frac{l}{l_0}\right)^5 \epsilon, \tag{29}$$

the drain νS^2 being partitioned between the dissipation ϵ and the backscatter. The resolved-scale energy equation contains a term due to the random accelerations which will have a mean value equal to this backscatter. For algebraic simplicity we will rewrite the subgrid energy equation as

$$\nu S^2 (1 - C_2) = \epsilon = C_1 \frac{E^{\frac{3}{2}}}{l}, \tag{30}$$

where C_2 is a constant simply related to $C_B(l/l_0)^5$ and we also note the fact that the subgrid-scale energy E is related to ϵ and l. In the absence of backscatter the value of C_1 is determined by the stress–energy ratio. For completeness we also note the local equilibrium equation for subgrid scalar variance E_θ, i.e.

$$\nu \frac{D^2}{Pr}(1 - D_2) = \epsilon_\theta = D_1 \frac{E^{\frac{1}{2}} E_\theta}{l}, \tag{31}$$

where D_2 is the constant analogous to C_2, and D_1 is a constant which is determined, in the absence of backscatter, by the stress–energy ratio, the scalar–flux correlation coefficient and the Prandtl number.

We now follow the analysis of Lilly (1967). In the interior of the flow we assume the filter scale falls within a long inertial subrange with spectra $E^{(u)}(k) = \alpha \epsilon^{\frac{2}{3}} k^{-\frac{5}{3}}$ and $E^{(\theta)}(k) = \beta \epsilon^{-\frac{1}{3}} \epsilon_\theta k^{-\frac{5}{3}}$ for the energy and passive scalar variance. Observations give values of α and β of about 1.5 and 0.7 (Lesieur 1987). We then consider integrals over a spherical filter volume, i.e.

$$E = \int_{\pi/l_f}^{\infty} E^{(u)} \, \mathrm{d}k = \tfrac{3}{2} \alpha \epsilon^{\frac{2}{3}} \left(\frac{l_f}{\pi}\right)^{\frac{2}{3}}, \tag{32}$$

$$\overline{S^2} = 2 \int_0^{\pi/l_f} k^2 E^{(u)} \, \mathrm{d}k = \tfrac{3}{2} \alpha \epsilon^{\frac{2}{3}} \left(\frac{l_f}{\pi}\right)^{-\frac{4}{3}} \tag{33}$$

and

$$\tfrac{1}{2} E_\theta = \int_{\pi/l_f}^{\infty} E^{(\theta)} \, \mathrm{d}k = \tfrac{3}{2} \beta \epsilon^{-\frac{1}{3}} \epsilon_\theta \left(\frac{l_f}{\pi}\right)^{\frac{2}{3}}, \tag{34}$$

$$\overline{D^2} = 2 \int_0^{\pi/l_f} k^2 E^{(\theta)} \, \mathrm{d}k = \tfrac{3}{2} \beta \epsilon^{-\frac{1}{3}} \epsilon_\theta \left(\frac{l_f}{\pi}\right)^{-\frac{4}{3}}. \tag{35}$$

Note that $E^{(u)}$ integrates to the total energy whilst $E^{(\theta)}$ integrates to half the scalar variance. These results only apply in an ensemble mean and, in detail, for a spherical filter. The conventional Lilly analysis notes that

$$\epsilon = l^2 S^3, \tag{36}$$

$$\epsilon_\theta = l^2 S D^2 / Pr. \tag{37}$$

With backscatter we now have

$$\epsilon = l^2 S^3 (1 - C_2), \tag{38}$$

$$\epsilon_\theta = l^2 S D^2 (1 - D_2)/Pr \tag{39}$$

and, if in the flow interior we take $l = l_0$ and $l_f = l_0/C_f$, we obtain

$$C_f^2(1 - C_2) = \frac{1}{\pi^2 (\frac{3}{2}\alpha)^{\frac{3}{2}}}, \quad \frac{C_1}{C_f} = \frac{\pi}{(\frac{3}{2}\alpha)^{\frac{3}{2}}}, \tag{40}$$

$$C_f^2(1 - D_2) = \frac{Pr}{\pi^2 (\frac{3}{2})^{\frac{3}{2}} \alpha^{\frac{1}{2}} \beta}, \quad \frac{D_1}{C_f} = \frac{\pi}{2(\frac{3}{2})^{\frac{3}{2}} \alpha^{\frac{1}{2}} \beta} \tag{41}$$

and

$$Pr = \frac{\beta (1 - D_2)}{\alpha (1 - C_2)}. \tag{42}$$

This gives $C_f = C_{f0}(1 - C_2)^{-\frac{1}{2}}$, $C_1 = C_{10}(1 - C_2)^{-\frac{1}{2}}$, $Pr = Pr_0(1 - D_2)/(1 - C_2)$ and $D_1 = D_{10}(1 - C_2)^{-\frac{1}{2}}$, where C_{f0}, C_{10}, Pr_0, and D_{10} are the values with $C_2 = D_2 = 0$. With backscatter C_f, C_1 and D_1 are thus increased. These results enable us to estimate E and E_θ from

$$\epsilon = C_1 \frac{E^{\frac{3}{2}}}{l} = \frac{C_{10}}{(1 - C_2)^{\frac{1}{2}}} \frac{E^{\frac{3}{2}}}{l} \tag{43}$$

and

$$\epsilon_\theta = D_1 \frac{E^{\frac{1}{2}} E_\theta}{l} = \frac{D_{10}}{(1 - C_2)^{\frac{1}{2}}} \frac{E^{\frac{1}{2}} E_\theta}{l}. \tag{44}$$

The Prandtl number is seen to depend on the value of C_2 and D_2 and we note that, in contrast to the value of $Pr_0 = 0.47$ which follows from values of $\alpha = 1.5$ and $\beta = 0.7$ in the absence of backscatter, the value obtained with backscatter ($C_B = 1.4$, $C_{B\theta} = 0.45$) is 0.77. We have taken Pr to be a constant (0.7) rather than the value given by (42). The constant value taken for Pr happens to nearly match (42) in the flow interior (for $C_B = 1.4$, $C_{B\theta} = 0.45$) and surface-layer observations close to the ground. If (42) were strictly enforced then Pr would be unrealistic close to the surface. The increase in C_f from C_{f0} to $C_{f0}/(1 - C_2)^{\frac{1}{2}}$ suggests that with backscatter we are reducing the filter scale if we keep l_0 a constant. It suggests that we should, for equal ratio of filter to mesh, change l_0 to $l_0/(1 - C_2)^{\frac{1}{2}}$ as we alter C_2. Taking our view of filters and meshes, this has implications for numerical accuracy and the scale on which the backscatter random stresses should be filtered. In the near-surface region, where l changes from l_0 to κz, we use (20) to estimate how the backscatter should vary with height. The arguments leading to (20) assumed a fixed filter scale l_f which is proportional to l_0. Here there is a suggestion that, since C_2 varies in the matching region, perhaps the ratio l_0/l_f should also be varied and lead to a modification of (20). However, the Lilly analysis is wholly inappropriate to the near-surface region and we have not sought to modify (20) in consequence of it. Even in the flow interior the analysis has many assumptions and should not be relied on quantitatively. We have however used (43) and (44) to estimate the subgrid-scale energy and scalar variance in our simulations, with ϵ and ϵ_θ given by (38) and (39) and with C_{10} and D_{10} taken to be the values of C_1 and D_1 used in the simulations without backscatter. The values of E and E_θ thus obtained are, for fixed ϵ and ϵ_θ, a factor of $(1 - C_2)^{\frac{1}{3}}$ smaller than those obtained in the absence of backscatter. Given the uncertainty in the correct values for C_1 and D_1 this is a secondary issue. We note the need for a better theoretical basis for these changes.

5. Backscatter results

The backscatter model has been applied in simulations of the neutral static stability planetary boundary layer. Figure 5 shows the resulting vertical profiles of non-dimensional velocity shear and passive scalar gradient. These were obtained with $n = 2$ in the wall-match equation and a value of $C_B = 1.4$. They can be compared with the profiles in figure 3 obtained without backscatter. The simulation with backscatter has a realistic velocity profile. The scalar profile is also very much improved and we note the possibility that an accurate profile might require the Prandtl number in the subgrid model to vary in the matching region. In the flow interior a value based on inertial subrange data would seem appropriate whilst close to the wall a value based on boundary-layer behaviour might be correct. We have maintained a constant value of 0.7 which is typical of a boundary layer and perhaps consistent with the above analysis of how backscatter alters Pr in the inertial subrange. As noted above the improved scalar profile does not imply that we have used the correct value of $C_{B\theta}$. Owing to the linearity of the scalar variable the scalar backscatter has no influence on the mean scalar profile and the profile behaviour only allows a judgement of the value of C_B.

The inclusion of backscatter seems remarkably successful in eliminating the obvious errors in the matching region. The precise agreement obtained depends on the choice of $C_B = 1.4$ and on the choice of $n = 2$. With other parameters fixed the value of the velocity gradient in the matching region varies steadily with C_B. Thus a value of $C_B = 0.5$ was found to only half-eliminate the errors whilst a value of $C_B = 2.0$ leads to non-dimensional gradients as small as 0.5. The power n has its main influence on the shape of the profile in the matching region so that with $n = 1$ the non-dimensional gradients remain slightly too big very close to the surface. A test of altering the factor $(l/l_0)^5$ (equation (20)) to a factor $(l/l_0)^2$ showed that this factor, like the power n, affected the profile shape. With a factor of $(l/l_0)^2$ the non-dimensional shear reduced below unity in a small region close to the surface. The profiles in figure 5 show a tendency for the non-dimensional gradients to take a value slightly less than unity close to the surface. This may be a consequence of seeking to impose the von Kármán constant at a value of 0.4 on a pointwise basis. At the height of the lowest grid point this will lead to an area-average value of κ approximately equal to $0.4(1+\sigma_u^2/2U_\Delta^2+\sigma_v^2/4U_\Delta^2)$, where U_Δ is the mean horizontal velocity at the lowest height and σ_u and σ_v are the standard deviations of the x- and y-components of the velocity at the same height. The correction is about 2% and accounts for the non-dimensional gradients being slightly less than unity. Indeed it is clear that a refined attempt to determine C_B and n (in (9)) would need to address this issue of local values of the von Kármán constant. We may have already made some implicit allowance in our choice of n and C_B.

This correction of the velocity profile would, in itself, be expected to have a large influence on the flow. In the simulation without backscatter the surface stress u_*^2 has a value of 0.141 (geostrophic drag coefficient $C_G = 1.41 \times 10^{-3}$) while with backscatter the surface stress increases to 0.189 ($C_G = 1.89 \times 10^{-3}$). This latter value is in better agreement with observations, with the Rossby number similarity coefficients estimated by Grant (1986) suggesting a value of $C_G = 2.0 \times 10^{-3}$ for these conditions. We note the restrictive resolution and upper boundary conditions used in the present study and do not seek detailed comparison with planetary-boundary-layer data.

Figure 6 shows the variances of the velocity components from the simulation with backscatter. The profile of σ_u^2 has been dramatically changed and no longer has an

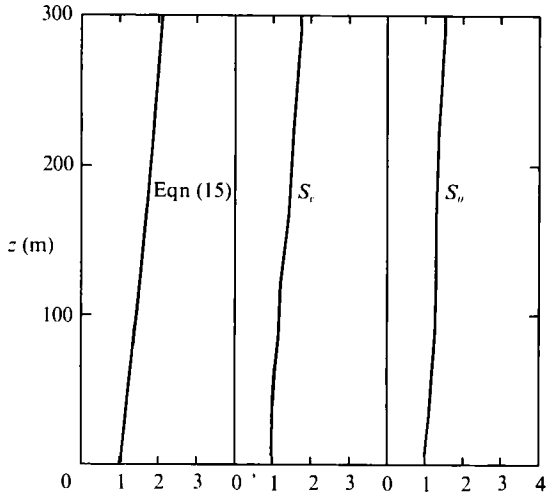

FIGURE 5. Profiles of the non-dimensional shear and passive scalar gradient from the planetary-boundary-layer simulation with backscatter. Also shown is the non-dimensional shear obtained from a mixing-length solution with the mixing-length given by (15).

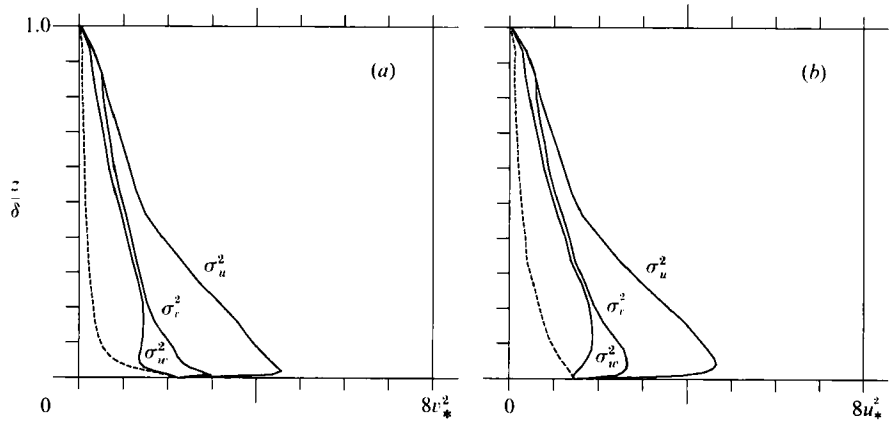

FIGURE 6. Profiles of the velocity variances σ_u^2, σ_v^2 and σ_w^2 from the planetary-boundary-layer simulation with backscatter. Solid lines: total variance; dashed line: subgrid part. (*a*) Results with an isotropic estimate of the subgrid contributions based on (43); (*b*) results using subgrid estimates of σ_w^2 based on the Kansas data as described in the text.

unrealistic near-surface peak. The value close to the surface is however unrealistic due to the isotropic estimate of subgrid variance. In contrast to the case without backscatter the resolved-scale contribution is not so large as to prevent a match with the expected value of 5 to 6 times u_*^2. The changes to the σ_v^2 profile are less marked and the profile remains consistent with a surface value of about $2.5u_*^2$. The profile of σ_w^2 shows values in the flow interior which are generally larger than in the simulation without backscatter and are consistent with observed profiles (Grant 1986) and an expected near-surface value of 1.4 to 1.8 times u_*^2. The slight local minimum of σ_w^2 in the matching region remains. We attribute this to the inadequate subgrid-scale energy estimates, which as well as assuming an isotropic energy distribution, make no allowance (other than that caused by the variation of C_2 in (43)) for the variation in the subgrid stress–energy ratio as the surface is approached.

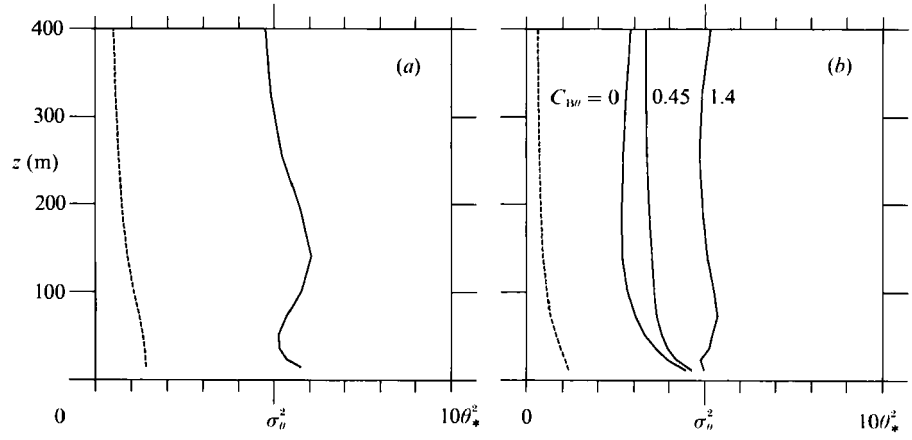

FIGURE 7. Profiles of the scalar variance σ_θ^2 from the planetary-boundary-layer simulations. Solid lines: total variance, dashed lines: subgrid part. (*a*) Results obtained without backscatter; (*b*) results obtained using backscatter. In (*b*) the subgrid component is only shown for $C_{B\theta} = 0.45$. The other three curves show σ_θ increasing with $C_{B\theta}$ for $C_{B\theta} = 0$, 0.45 and 1.4.

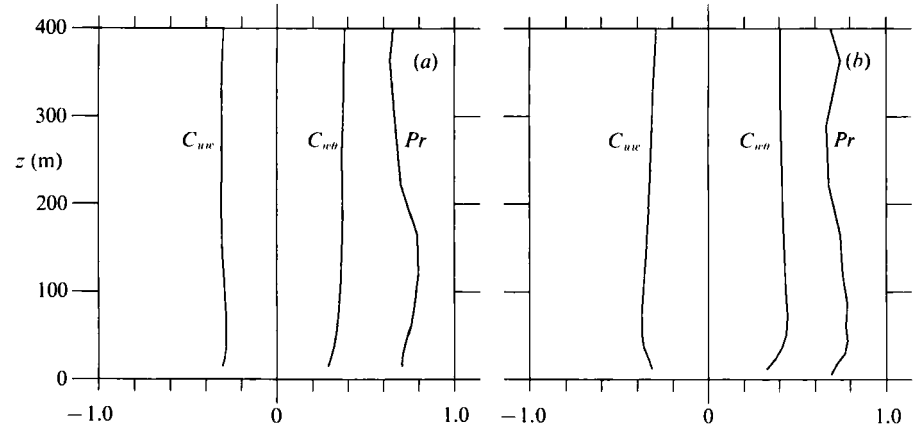

FIGURE 8. Profiles of the turbulent Prandtl number, the correlation coefficient of u and w, and the correlation coefficient of w and θ from the planetary-boundary-layer simulations. (*a*) Results obtained without backscatter; (*b*) results obtained using backscatter with $C_{B\theta} = 0.45$.

From the observed (Kaimal *et al.* 1972) spectra of σ_w^2 and $\overline{uw}$ in the atmospheric surface layer we see that filtering at a scale comparable with the peak of the w-spectrum gives a large fraction of total energy as subgrid scale but only a small fraction of the stress as subgrid scale. In the matching region we are thus underestimating the subgrid values of σ_w^2 by assuming the value typical of the whole spectrum. It is possible to use the observed spectra to provide an improved estimate of σ_w^2. By comparing the fraction of the shear stress which is subgrid with integrals of the observed $\overline{uw}$ spectrum a filter scale can be deduced. This value of filter scale can then be applied to the σ_w^2 spectrum to deduce an appropriate estimate of subgrid-scale σ_w^2. Details of this procedure are given in Appendix B. These estimates should be an improvement upon those based on (14) or (43) but are, as noted in the Appendix, still subject to various assumptions. The low-frequency parts of atmospheric σ_u^2 and σ_v^2 spectra are not as well defined as those of σ_w^2 and we have not

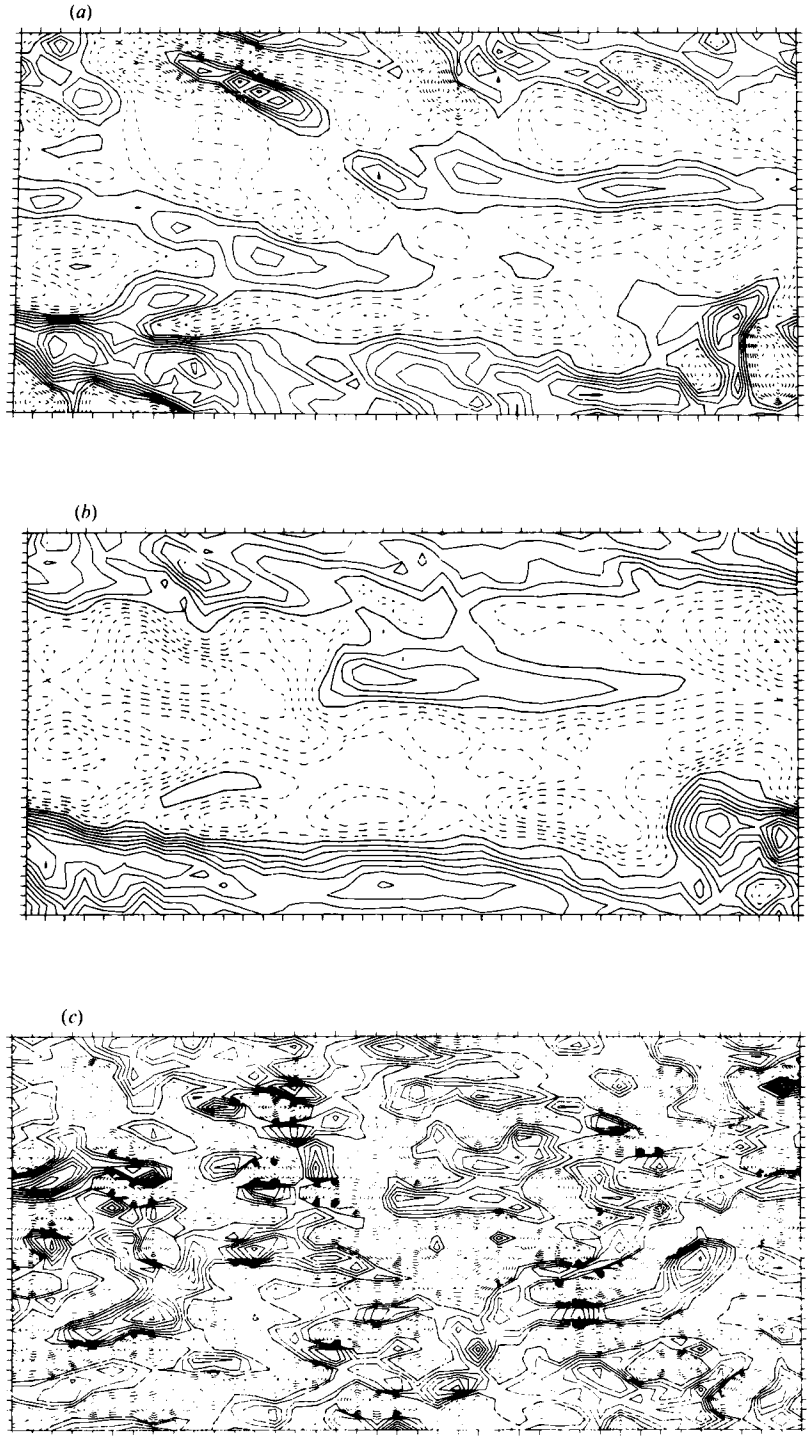

FIGURE 9(*a–c*). For caption see facing page.

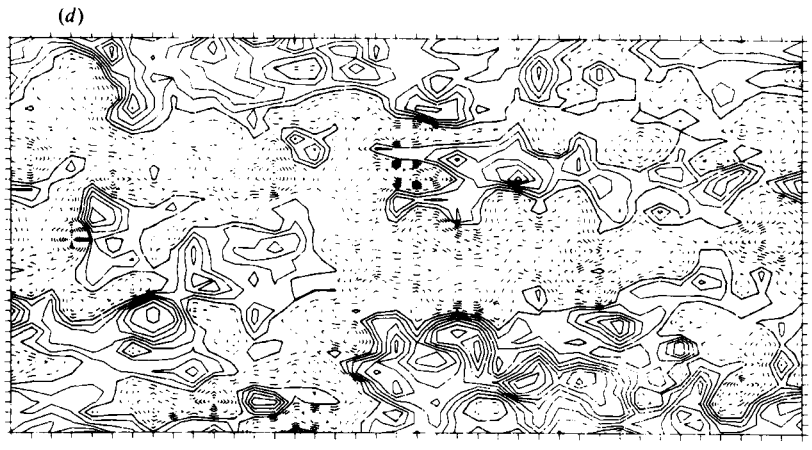

FIGURE 9. Contour plots of horizontal sections of the w and $\theta-\langle\theta\rangle$ fields obtained at $z = 86$ m. (a, b) Show the w and $\theta-\langle\theta\rangle$ fields respectively without backscatter; (c, d) again show the w and $\theta-\langle\theta\rangle$ fields respectively using backscatter with $C_{\mathrm{B}\theta} = 0.45$. In each plot the contour interval is a tenth of the maximum absolute value of the field and the dashed lines show negative values.

attempted to use similar procedures to obtain estimates of the subgrid parts of σ_u^2 and σ_v^2. Figure 6(b) shows the variances of all three velocity components with this subgrid estimate of σ_w^2 used with each. The high-frequency parts of the σ_u^2 and σ_v^2 spectra match the σ_w^2 spectrum and, away from the surface, the σ_w^2 estimate should apply to all these spectra. Close to the surface the total variance in σ_u^2 and σ_v^2 will be in error. The improvement seen in figure 6(b) suggests that our diagnosis of the σ_w^2 minimum was correct. A modest maximum now appears. We believe that the correct behaviour may be a simple increase towards the surface but observations (Högström 1990) do invariably seem to show some increase in σ_w^2 with height in the near-surface region. To do justice to the details of these profiles, a simulation with greater resolution is needed.

We have noted that the scalar backscatter does not influence the mean scalar profile. The direct effect of the scalar backscatter is to increase the scalar variance and any judgement of the value of $C_{\mathrm{B}\theta}$ for a passive scalar has to be based on the behaviour of statistics involving the scalar variance. We present results obtained with three values of $C_{\mathrm{B}\theta}$, namely 1.4, 0.45 and 0.0 ($C_{\mathrm{B}} = 1.4$ in all cases). Figure 7(a) shows profiles of the scalar variance obtained in the original simulation without backscatter and figure 7(b) shows the various cases with backscatter. For clarity the subgrid-scale contribution in figure 7(b) is only shown with $C_{\mathrm{B}\theta} = 0.45$. The subgrid-scale contribution is based on (14) in the case without backscatter and on (44) in the cases with backscatter. These estimates are based on inertial-subrange assumptions and, although they may be realistic in the flow interior, are not appropriate near the surface. The shape of the scalar variance profile is not expected to exactly match the σ_u^2 profile. Apart from dynamical differences, the different shapes of the shear stress and scalar flux profiles imposed here are a large influence. In contrast to the near-linear decrease of stress with height, in consequence of the constant-temperature upper boundary condition the scalar flux is constant with height in these simulations. A further difference arises at the surface, where in consequence of the constant-heat-flux boundary condition the resolved scalar fluctuations are a maximum at $z = 0$. Without backscatter there is an unrealistic maximum which occurs at the matching height and which we believe to be associated with mean scalar gradient errors at that

height. In the cases with backscatter and $C_{B\theta} = 0$ or 0.45, the unrealistic maximum has been removed and we see a more smoothly varying profile with a surface maximum. Increasing $C_{B\theta}$ leads to an increase in the values of σ_θ^2. A typical value of $\sigma_\theta^2/\theta_*^2$ in a neutral surface layer is about 5 (Smith & Anderson 1984) but the profile and exact value is not so well known as to allow a judgement of the optimum value of $C_{B\theta}$. With $C_{B\theta} = 1.4$ the increase in σ_θ^2 does not seem particularly excessive but in the matching region a maximum of σ_θ is caused by the temperature backscatter. This seems unrealistic and is consistent with the view that $C_{B\theta}$ should be less than C_B.

The conclusion here is that the backscatter has had entirely beneficial effects. The greatest effects of the backscatter in the simulation are confined to the features shown. Other statistics show little modification and in view of the previous general success of large-eddy simulations this is reassuring.

As a further illustration of the changes produced, figure 8 shows profiles of the turbulent Prandtl number, the correlation coefficient of u and w (C_{uw}), and the correlation coefficient of w and θ ($C_{w\theta}$). Figure 8 (*a*) shows the case without backscatter and figure 8 (*b*) the case with backscatter, with $C_B = 1.4$ and $C_{B\theta} = 0.45$. These quantities have been derived with the inclusion of the subgrid-scale statistics. This is straightforward in the case of the Prandtl number, where only fluxes are involved, but for the correlation coefficients we have used the isotropic subgrid energy estimate based on (14), (43) and (44) as appropriate and some near-surface errors must be expected. The Prandtl number does not seem to be significantly influenced by backscatter. Noting that the subgrid-scale value of 0.7 is forced at the surface, the simulations suggest that the Prandtl number should have a surface value of about 0.8 decreasing to 0.6 in the middle of the boundary layer. The correlation coefficient of u and w has a near-constant interior value of about -0.3 both with and without backscatter. Without backscatter the values show a weak near-surface minimum which is probably due to the excessive values of σ_u^2 which occur near the surface in that simulation. With backscatter there is a weak near-surface maximum which is associated with errors in subgrid-scale estimates and the minimum of σ_w^2 at that height. The correlation coefficient for w and θ has a near-constant interior value of about 0.4 in the simulation with backscatter. This decreases close to the surface due to the increase in σ_θ^2 and the erroneously large subgrid estimate for σ_w^2 at the surface caused by using (43). Without backscatter this correlation coefficient is reduced by the larger values of σ_θ^2. The differences seen between the profiles in figures 8 (*a*) and 8 (*b*) are small and both results show fair agreement with observations.

We conclude the presentation of results with an examination of the velocity and scalar fields. Figure 9 shows horizontal sections of the vertical velocity and scalar fields at a level within the matching region where backscatter is significant. Figures 9 (*a*) and 9 (*b*) show these fields for the case without backscatter and figures 9 (*c*) and 9 (*d*) show the fields with backscatter ($C_B = 1.4$. $C_{B\theta} = 0.45$). Without backscatter the fields are fairly smooth and evidence of a distinct elongated structure which spans the domain is seen in the scalar field. With backscatter the fields have much finer scales present and we would judge them to be a little rough for good finite-difference approximation. The plotting routine uses only linear interpolation and does not mask rough features. The tendency to generate elongated structures is seen to be diminished and two-point correlations (not shown) are more circular.

Figure 10 shows vertical sections of the vertical velocity field, without (figure 10 *a*) and with backscatter (figure 10 *b*). There is a general tendency towards smaller scales throughout the flow but large differences are confined to the near-surface region where eddies now penetrate much closer to the wall.

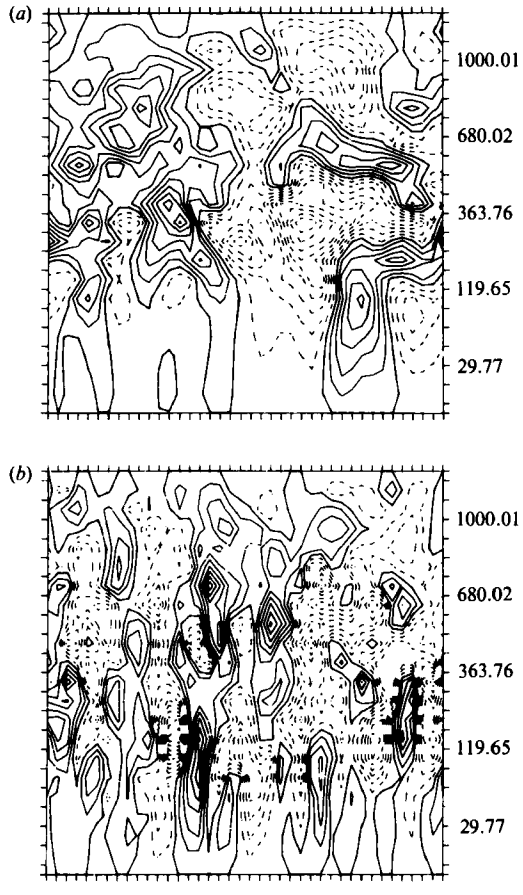

FIGURE 10. Contour plots of (y, z) sections of the w-field. (*a*) Results obtained without backscatter; (*b*) results obtained using backscatter. The contour interval is a tenth of the maximum absolute value of the field and the dashed lines show negative values.

From this examination of the velocity fields we must express some concern that the backscattered energy has lead to slightly rough fields which may give some finite-difference errors. The fields obtained with the Smagorinsky model were fairly smooth; however, the analysis suggests that with l_0 fixed we have reduced the filter scale. There may therefore be a requirement to increase the ratio of l_0 to the mesh spacing (i.e. C_s) with backscatter. It is also possible that we have not adequately filtered the random stress field and have consequently input too much energy on the shortest scales. We note that, from the tests shown in §3, reducing l_0 did not have beneficial effects, and so we are confident that the improvements found with backscatter are not just a consequence of effectively altering l_0 or C_s.

6. Conclusions

Previous large-eddy simulations of high-Reynolds-number boundary layers suffer from a common problem of excessive mean velocity gradients close to the surface. A series of test simulations suggest that whatever near-surface mixing-length variation is adopted this error is inherent in the Smagorinsky subgrid model. Noting that stochastic backscatter is a physical process which is missing from the Smagorinsky

model and which should be important in this region, a Smagorinsky–backscatter model is proposed and tested. The backscatter appears to remedy the problem and leads to an improved large-eddy simulation. Support that backscatter is the correct cure of the problem is provided by the theoretical support for the magnitude of the effect. The magnitude found to give optimum results is an energy backscatter which, where lengthscales are not influenced by walls, has a value of 1.4 times the dissipation. This value is equal to that obtained from EDQNM theory for an infinite inertial subrange (J. R. Chasnov, private communication giving the evaluation of the integrals in Chasnov 1991). In the case of a passive scalar the backscatter in the scalar equation does not influence the mean scalar profile but, rather, the scalar variance and related statistics. The results obtained support the theoretical suggestion that the backscatter of half the scalar variance is a relatively smaller fraction of the scalar dissipation. The precise value of scalar coefficient could not be determined and we note that future applications with buoyant scalars may provide a more sensitive test.

This paper has demonstrated a credible cure to a long-standing problem with an improvement to the Smagorinsky subgrid model so as to include stochastic backscatter. It is perhaps especially significant that the velocity gradient problem did not improve with increased resolution. Without remedy, this problem would seriously impair the value of high-Reynolds-number simulations. The success of the backscatter model gives hope that the optimism concerning the many future applications of large-eddy simulation is well founded.

Future high-resolution studies should allow more careful refinement of the stochastic model. In particular it would seem desirable to quantify the backscatter process by analysis of high-resolution velocity fields in either direct or large-eddy simulations.

Appendix A. The EDQNM prediction for $C_{B\theta}/C_B$

Following Chasnov's (1991) work with the velocity field we can estimate the backscatter rate of (half) scalar variance from the EDQNM approximation. We restrict attention to the flow interior where the filter scale lies in the inertial subrange. The EDQNM approximation then gives a rate of change of $E^{(\theta)}(k)$ resulting from the backscatter which equals

$$\iint \mathrm{d}p\,\mathrm{d}q\,\theta^{(\theta)}_{kpq}\frac{k^3}{pq}(1-y^2)\,E^{(u)}(q)\,E^{(\theta)}(p) \tag{A 1}$$

(Lesieur 1987, p. 147), the integration being over the part of the region $|p-q| \leqslant k$ where either p or q exceeds the spectral cut. The notation here is as in Chasnov's paper, but with superscripts $^{(u)}$ and $^{(\theta)}$ being used to distinguish quantities corresponding to the velocity and scalar fields. Equation (A 1) is the analogue of Chasnov's equation (11). This could be evaluated numerically, but we content ourselves with evaluating the asymptotic form which occurs when k is much less than the spectral cut. This leads to a spectral backscatter rate given by

$$\tfrac{4}{3}k^4\int_{\pi/l_t}^{\infty}\mathrm{d}p\,\theta^{(\theta)}_{0pp}\frac{E^{(u)}(p)E^{(\theta)}(p)}{p^2} \tag{A 2}$$

(see Lesieur, 1987, p. 153), where we have assumed a sharp spectral cut at

wavenumber π/l_f as in the Lilly analysis presented in §4. Comparing this with Chasnov's equation (18) yields

$$\frac{C_{B\theta}}{C_B} = \frac{10}{7}\frac{\beta}{\alpha}\frac{1}{3Pr}, \tag{A 3}$$

where we have taken the timescale ratio $\theta^{(\theta)}_{0pp}/\theta^{(u)}_{0pp}$ to the $1/(3Pr)$ as is usual (Lesieur 1987, p. 146). With $\alpha = 1.5$, $\beta = 0.7$ and $Pr = 0.7$, equation (A 3) gives $C_{B\theta} = 0.32C_B$.

Appendix B. Calculation of subgrid σ_w^2 using the Kansas data

Data collected by Kaimal *et al.* (1972) during the Kansas experiment show that the surface-layer w-spectra and uw-cospectra are well described by

$$nS_w(n) = \frac{2u_*^2 f}{1+5.3f^{\frac{5}{3}}}, \quad nC_{uw}(n) = \frac{14u_*^2 f}{(1+9.6f)^{2.4}}, \tag{B 1}$$

where n denotes frequency and $f = nz/\bar{u}$. If the filter scale corresponds to a frequency n_f then we would expect the fractions of σ_w^2 and $\overline{uw}$ which are subgrid to be

$$\int_{n_f}^{\infty} S_w(n)\,\mathrm{d}n \Big/ \int_0^{\infty} S_w(n)\,\mathrm{d}n \tag{B 2}$$

and

$$\int_{n_f}^{\infty} C_{uw}(n)\,\mathrm{d}n \Big/ \int_0^{\infty} C_{uw}(n)\,\mathrm{d}n. \tag{B 3}$$

Using the known fraction of subgrid stress we can therefore estimate n_f, and hence the fraction of σ_w^2 which is subgrid.

REFERENCES

Bardina, J., Ferziger, J. H. & Reynolds, W. C. 1983 Improved turbulence models based on large eddy simulation of homogeneous, incompressible, turbulent flows. *Rep.* TF-19. Thermosciences Division, Department of Mechanical Engineering, Stanford University.

Chasnov, J. R. 1991 Simulation of the Kolmogorov inertial subrange using an improved subgrid model. *Phys. Fluids* A **3**, 188–200.

Deardorff, J. W. 1970 A numerical study of three-dimensional turbulent channel flow at large Reynolds numbers. *J. Fluid Mech.* **41**, 453–480.

Grant, A. L. M. 1986 Observations of boundary layer structure made during the KONTUR experiment. *Q. J. R. Met. Soc.* **112**, 825–841.

Högström, U. 1990 Analysis of turbulence structure in the surface layer with a modified similarity formulation for near neutral conditions. *J. Atmos. Sci.* **47**, 1949–1972.

Kaimal, J. C., Wyngaard, J. C., Izumi, Y. & Coté, O. R. 1972 Spectral characteristics of surface layer turbulence. *Q. J. R. Met. Soc.* **98**, 563–589.

Kraichnan, R. H. 1976 Eddy viscosity in two and three-dimensions. *J. Atmos. Sci.* **33**, 1521–1536.

Leith, C. E. 1990 Stochastic backscatter in a subgrid-scale model: plane shear mixing layer. *Phys. Fluids* A **2**, 297–299.

Lesieur, M. 1987 *Turbulence in Fluids*. Martinus Nijhoff.

Leslie, D. C. & Quarini, G. L. 1979 The application of turbulence theory to the formulation of subgrid modelling procedures. *J. Fluid Mech.* **91**, 65–91.

Lilly, D. K. 1967 The representation of small-scale turbulence in numerical simulation experiments. *Proc. Tenth IBM Scientific Computing Symp. on Environmental Sciences, Thomas J. Watson Research Center, Yorktown Heights*, pp. 195–210.

MASON, P. J. 1989 Large-eddy simulation of the convective atmospheric boundary layer. *J. Atmos. Sci.* **46**, 1492–1516.

MASON, P. J. & CALLEN, N. S. 1986 On the magnitude of the subgrid-scale eddy coefficient in large-eddy simulations of turbulent channel flow. *J. Fluid Mech.* **162**, 439–462.

MASON, P. J. & THOMSON, D. J. 1987 Large-eddy simulations of the neutral-static-stability planetary boundary layer. *Q. J. R. Met. Soc.* **113**, 413–443.

MOIN, P. & KIM, J. 1982 Numerical investigations of turbulent channel flow. *J. Fluid Mech.* **118**, 341–377.

PIACSEK, S. A. & WILLIAMS, G. P. 1970 Conservation properties of convection difference schemes. *J. Comput. Phys.* **6**, 392–405.

PIOMELLI, U., MOIN, P. & FERZIGER, J. H. 1988 Model consistency in large eddy simulation of turbulent channel flows. *Phys. Fluids* **31**, 1884–1891.

SMAGORINSKY, J. 1963 General circulation experiments with the primitive equations: 1. The basic experiment. *Mon. Weather Rev.* **91**, 99–164.

SMITH, S. D. & ANDERSON, R. J. 1984 Spectra of humidity, temperature and wind over the sea at Sable Island, Nova Scotia. *J. Geophys. Res.* **89**, 2029–2040.

WOOD, N. & MASON, P. J. 1991 The influence of static stability on the effective roughness lengths for momentum and heat transfer. *Q. J. R. Met. Soc.* **117**, 1025–1056.